Journal of the Taiwan Institute of Chemical Engineers 107 (2020) 152–160

Contents lists available at ScienceDirect

Journal of the Taiwan Institute of Chemical Engineers

journal homepage: www.elsevier.com/locate/jtice

Trifluoroethylene bond enrichment in P(VDF-TrFE) copolymers with enhanced ferroelectric behaviors by plasma fluorination on bottom electrode

Jer-Chyi Wang[a,b,c,*], Yi-Pei Jiang[a], Yu-Jie Lin[a], Shun-Hsiang Chan[d,e], Ming-Chung Wu[d,e,f,**]

[a] Department of Electronic Engineering, Chang Gung University, Guishan Dist., 33302 Taoyuan, Taiwan
[b] Department of Neurosurgery, Chang Gung Memorial Hospital, Linkou, Guishan Dist., 33305 Taoyuan, Taiwan
[c] Department of Electronic Engineering, Ming Chi University of Technology, Taishan Dist., 24301 New Taipei City, Taiwan
[d] Department of Chemical and Materials Engineering, Chang Gung University, Guishan Dist., 33302 Taoyuan, Taiwan
[e] Green Technology Research Center, Chang Gung University, Guishan Dist., 33302 Taoyuan, Taiwan
[f] Division of Neonatology, Department of Pediatrics, Chang Gung Memorial Hospital, Linkou, Guishan Dist., 33305 Taoyuan, Taiwan

ARTICLE INFO

Article history:
Received 25 May 2019
Revised 7 October 2019
Accepted 5 November 2019
Available online 12 December 2019

Keywords:
P(VDF-TrFE)
CF_4 plasma
Ferroelectric
Remanent polarization
Fatigue

ABSTRACT

CF_4 plasma treatment on n^+-Si wafers as bottom electrodes (BEs) of poly(vinylidene fluoride-co-trifluoroethylene) (P(VDF-TrFE)) metal-ferroelectric-metal (MFM) capacitors has been investigated in this study. Prior to the fabrication of MFM capacitors, comprehensive material analyses are administered to identify the incorporation of fluorine atoms into P(VDF-TrFE) copolymers, revealing an enrichment in C_2HF_3 (trifluoroethylene) bonds and an improvement in the crystallinity of the film. The P(VDF-TrFE) MFM capacitors with CF_4-plasma-treated n^+-Si wafers show a shallower charge trapping level of 0.154–0.226 eV extracted from the Frenkel–Poole (*F–P*) emission at 213–273 K for the BE injection compared to that for the top electrode (TE) injection, which is ascribed to the passivation of deep traps by the fluorine atoms that diffused from the n^+-Si wafers. Thus, asymmetric remanent polarization and a negative internal bias field are obtained because of the significant increase in the β-phase at the bottom of the P(VDF-TrFE) films. With the CF_4 plasma treatment for 1 min, the P(VDF-TrFE) MFM capacitors demonstrate a remanent polarization ($2P_r$) of 6.58 μC/cm^2, a coercive electric field (E_c) of 0.47 MV/cm and stability for more than 3×10^4 cycles with negligible fatigue, making the fluorine-incorporated P(VDF-TrFE) copolymers suitable for future high-performance nonvolatile memory applications.

1. Introduction

Recently, organic ferroelectric materials have attracted considerable attention due to their advantages of flexibility, room-temperature fabrication, low cost, and a simple manufacturing process [1,2]. Among these materials, polyvinylidenefluoride (PVDF) homopolymer is one of the most promising candidates because of its unique properties, such as good mechanical elasticity, a high breakdown electric field, and self-healing ability [3–5]. The piezoelectricity of PVDF and its copolymers was first discovered by Kawai et al. [6] and was widely studied from 1980 [7]. As a semicrystalline homopolymer, PVDF comprises five crystalline phases, α-, β-, γ-, δ-, and ε-phases, depending on the fabricating process [8]. The α-, β-, and γ-phases are the most common chain conformation, and the β-phase is the polar phase with a large spontaneous polarization owing to the parallel arrangement of the C-F dipole moment [8–11]. The all trans (TTT) planar zigzag for the β-phase of PVDF can be obtained by the thermal or stress treatment of the as-deposited α-phase film with the trans-gauche conformation (TGTG') [12–14], exhibiting better pyro-, piezo-, and ferro-electric properties [8,15,16]. The ferroelectric properties have been proposed to originate from the large difference in electronegativity among fluorine, carbon and hydrogen, which have Pauling's values of 4.0, 2.5 and 2.1, respectively [17], where the electrons are attracted to the fluorine side of the polymer chain to create the polarization [18,19]. Compared to the PVDF homopolymer, the P(VDF-TrFE) copolymer, which is formed by the addition of some specific content of the trifluoroethylene (TrFE) monomer unit, increases the steric hindrance that favors a higher degree of crystallinity, playing an important role in the phase transition and nucleation behaviors [20]. With the TrFE monomers in the PVDF system, the interac-

* Corresponding author at: Department of Electronic Engineering, Chang Gung University, Guishan Dist., 33302 Taoyuan, Taiwan.
** Corresponding author at: Department of Chemical and Materials Engineering, Chang Gung University, Guishan Dist., 33302 Taoyuan, Taiwan.
E-mail addresses: jcwang@mail.cgu.edu.tw (J.-C. Wang), mingchungwu@cgu.edu.tw (M.-C. Wu).

https://doi.org/10.1016/j.jtice.2019.11.005
1876-1070/

tions between each unit and between dipole-to-dipole are reduced, resulting in a lower Curie temperature for the copolymer to be crystallized into the ferroelectric phase [21]. Consequently, the P(VDF-TrFE) presents a large remnant polarization ($2P_r$) [22], making it suitable for the applications in emerging memories [23], energy harvesters [24], nano-generators [25], and tactile sensors [26].

To enhance the ferroelectric behaviors of P(VDF-TrFE), some fabricating techniques, such as blending, annealing, doping and interface modification, have been implemented. For tuning the film composition, conventional P(VDF-TrFE) with 72.2/27.8 mol% and hydrogenated P(VDF-TrFE) with a low TrFE molar content of 9% have been synthesized to achieve a higher β-phase with a lower polymer chain length, corresponding to a larger grain size in its crystalline region [27]. In addition, low-temperature solvent vapor annealing can induce additional crystallization of the β-phase, leading to good ferroelectric and piezoelectric properties of P(VDF-TrFE) [28]. For the bilayer structure, devices with poly(methyl methacrylate) (PMMA) between the metal electrode and P(VDF-TrFE) film exhibit a larger ferroelectric polarization for a similar voltage drop owing to the improvement in the interface morphology [29]. It has also been reported that P(VDF-TrFE) and gold nanoparticles (Au-NPs) can be blended together for enhanced ferroelectric and piezoelectric characteristics, which are attributed to an increase in the effective electric field induced by the reduction in the effective volume of P(VDF-TrFE) for more aligned dipoles [30]. On the other hand, Mai et al. proposed that defects, imperfections, and grain boundaries within the ferroelectric materials serve as the pinning sites, hindering the switchable polarization because of the capture of charges by the pinning centers [31]; thus, the reliability properties, such as the cycling endurance of P(VDF-TrFE) films, are not sufficient [32]. The imperfections may be caused by the high-temperature and unsuitable solvent annealing, breaking the molecular bonds in the organic matrix, especially the C-F bonds [33], which have not been passivated to date. In this study, the characteristics of P(VDF-TrFE) MFM capacitors with CF_4-plasma-treated n^+-Si wafers are investigated. The material nature of P(VDF-TrFE) copolymers on CF_4-plasma-treated n^+-Si wafers is identified by X-ray photoelectron spectroscopy (XPS) depth profiling and X-ray diffractometer (XRD) patterns. By analyzing the conductive mechanisms at different bias polarities and temperatures, the energy band structures and charge trapping levels of the P(VDF-TrFE) MFM capacitors with CF_4-plasma-treated n^+-Si wafers are proposed, demonstrating the superior ferroelectric behaviors for future applications of organic materials in NVMs.

2. Experimental

2.1. Preparation of P(VDF-TrFE) MFM capacitors with CF_4-plasma-treated n^+-Si wafers

P(VDF-TrFE) MFM capacitors with CF_4-plasma-treated n^+-Si wafers as the bottom electrode (BE) were prepared. The wafers were first cleaned using the standard Radio Corporation of America (RCA) cleaning procedure. Then, the wafer surface was treated with CF_4 plasma at a radio-frequency (rf) power of 100 W for 1, 3 and 5 min by using an inductively coupled plasma (ICP) system (KD-ICP/RIE, KaoDuen Tech. Corp., Taipei, Taiwan). The working pressure of the chamber was 300 mTorr, and the gas flow of the CF_4 ambient was 300 sccm. Continuously, for the material synthesis, the P(VDF-TrFE) powder (70:30 mol%) provided by Piezotech S.A.S. (Arkema, Colombes, France) was dissolved in dimethylformamide (DMF) at a concentration of 5.0 wt%. The solution was spin-coated on the n^+-Si wafers at 750 rpm for 30 s in the glove box. The film thickness of the P(VDF-TrFE) measured by ellipsometry was approximately 350 nm. After the ferroelectric thin films had been formed, all samples were baked at 120 °C to dry the films and then annealed at 130 °C for 2 h on the hot plate to induce the crystallinity of the P(VDF-TrFE) films, especially the β-phase. Finally, a 300-nm-thick Al film was deposited by a thermal evaporator at 10^{-6} Torr with a pure Al bullet (99.999% purity), then defined lithographically and etched to form the top electrode (TE) with a diameter of 0.018 cm. Fig. 1 illustrates the schematic device structure and the entire fabrication process of the P(VDF-TrFE) MFM capacitors with CF_4-plasma-treated n^+-Si wafers.

2.2. Characterization of materials and devices

Following the CF_4 plasma treatment, the crystallinity of the PVDF-TrFE films on the CF_4-plasma-treated n^+-Si wafers was examined by X-ray diffractometer (XRD) using a Bruker D2 phaser system (Bruker AXS GmbH, Karlsruhe, Germany) with Cu Kα (8.04 keV) radiation as the excitation source. The composition of chemical bonds of the P(VDF-TrFE) films on n^+-Si wafers under different CF_4 plasma treatment conditions was detected by the X-ray photoelectron spectroscopy (XPS) using a VG ESCA scientific theta probe spectrometer (Thermo Fisher Scientific Inc., Waltham, MA, USA) with a pass energy of 50 eV at a take-off angle of 53° and Al Kα (1486.6 eV) radiation as the excitation source. The F 1*s* depth profiling was performed by Ar ion sputtering with a controlled bias of 3 kV and a controllable sputter area of 2 × 2 mm^2 to obtain a depth resolution of 15 nm. For the device characterization, the current versus electric field (*I*–*E*) curves, the polarization versus electric field (*P*–*E*) hysteresis curves, and the capacitance and dissipation versus electric field (*C*–*E* and *D*–*E*) curves were measured with a Keithley 4200 semiconductor characterization system (Keithley Instruments, LLC, Solon, OH, USA). The ferroelectric behaviors of the P(VDF-TrFE) MFM capacitors were measured using the Positive-Up Negative-Down (PUND) method [34,35] and the leakage current of the devices was measured directly by the source measurement unit (SMU) of Keithley 4200 with the measuring conditions for step voltage and delay time of 0.1 V and 1 s, respectively. The voltage bias was applied on the Al TE and the BE was grounded.

3. Results and discussion

3.1. Material analyses of P(VDF-TrFE) films

Fig. 2(a) shows the XRD spectra of the P(VDF-TrFE) films on the untreated and treated n^+-Si wafers. The XRD patterns illustrate that the CF_4 plasma treatment on n^+-Si wafers has a strong effect on the crystallinity in P(VDF-TrFE) as shown by the changes in the intensity of the peak at $2\theta \approx 20°$. To evaluate the crystallinity of the fluorine-incorporated P(VDF-TrFE) films, a curve deconvolution method from the XRD pattern of different crystalline phases was performed in Fig. 2(a). From the deconvoluted curves, two distinct crystalline phases at 20.2° and 20.8°, belonging to γ(110)- and β(110/220)-phases [36,37], respectively, can be observed. Then, the proportion of crystalline β-phase (χ_β) is calculated using the following equation [38],

$$\chi_\beta = \frac{A_\beta}{A_{total}} \times 100\% \quad (1)$$

where A_{total} and A_β represent the total integrated areas of crystalline diffraction peaks and crystalline β-phase, respectively. With the increase in the CF_4 plasma treatment time, both the peak intensity and the proportion of crystalline β-phase of P(VDF-TrFE) films are remarkably enhanced. Furthermore, it is reported that the surface wettability of the underlayer is directly related to the film thickness by spin-coating technique [39], as revealed in the characteristics of P(VDF-TrFE) film thickness and water contact angle of n^+-Si wafers in Fig. 2(b). The water contact angle images shown in Fig. S1a–d were measured using the sessile drop method with a

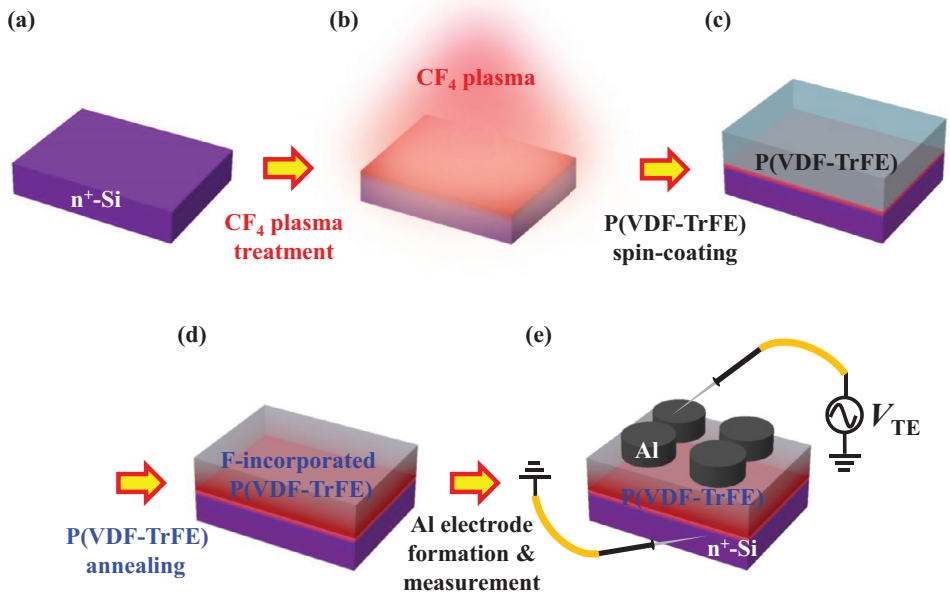

Fig. 1. Fabrication procedures of the P(VDF-TrFE) MFM capacitors with CF_4-plasma-treated n^+-Si bottom electrodes. (a) n^+-Si (100) wafers with standard RCA clean, (b) CF_4 plasma treatment on n^+-Si wafers in an inductively coupled plasma (ICP) system, (c) spin-coating P(VDF-TrFE) films, (d) thermal annealing at 130 °C for 2 h on the hot plate, and (e) Al electrode formation to fabricate the P(VDF-TrFE) MFM capacitors.

water droplet partially wetting the n^+-Si wafers [40,41]. It can be found that the water contact angle of the original n^+-Si wafer was 72°. After the CF_4 plasma treatment, the water contact angle of the n^+-Si wafers decreases dramatically and the wafer surface becomes more hydrophilic. The hydrophilic nature of the wafer surface contributes to the increase in the spin-coated P(VDF-TrFE) film thickness, as shown in Fig. 2(b).

Fig. 2(c) shows the C 1 *s* XPS spectra of the P(VDF-TrFE) films on CF_4-plasma-treated n^+-Si wafers. In this figure, there are four distinct peaks within the spectra. The C 1 *s* core level binding energies for poly-[$-CH_2-CF_2-$]-, *i.e.*, PVDF, are 286.3 ($C-H_2$) and 291.2 eV ($C-F_2$), while those for poly-[$-CF_2-CFH-$]–, *i.e.*, TrFE, are 287 (C–F) and 288.7 eV (C–FH) [42]. To understand the change of the peaks after the CF_4 plasma treatment, the XPS peak-area-ratios (PARs) of C–F, C–FH and $C-F_2$ bonds related to the $C-H_2$ bond are respectively calculated and illustrated in the bar chart of Fig. 2(c). It should be noted that the XPS PAR of the fluorinated carbon bonds increases with an increase in the CF_4 plasma treatment time, manifesting the reaction of fluorine atoms with the P(VDF-TrFE) films. Furthermore, the depth profiles of F 1 *s* XPS spectra taken at different etching levels in the P(VDF-TrFE) films on the untreated and 1-min CF_4-plasma-treated n^+-Si wafers are presented in Fig. 2(d) and (e) respectively to investigate the diffusion of fluorine atoms from the n^+-Si wafers into the P(VDF-TrFE) films after annealing. We can observe the F 1 *s* peaks at 689.9 and 689.1 eV, indicating the C_2HF_3 (TrFE) and C-F (PVDF and TrFE) bonds, respectively [43,44]. For the pure P(VDF-TrFE) film, the spectra are almost identical throughout the film (Fig. 2(d)). On the other hand, the F 1 *s* peak at 689.9 eV increases significantly from the surface to the bulk of the P(VDF-TrFE) film on the 1-min CF_4-plasma-treated n^+-Si wafer, implying that some imperfect TrFE and $C-H_2$ bonds of PVDF are passivated by the fluorine atoms from the CF_4-plasma-treated n^+-Si wafers to achieve the increased intensity of the C_2HF_3 bond. The depth profiles of the F 1 *s* XPS spectra in the P(VDF-TrFE) films on 3- and 5-min CF_4-plasma-treated n^+-Si wafers were also investigated and are shown in Fig. S2a,b, respectively. For the films on n^+-Si wafers with longer CF_4 plasma treatment times, more fluorine atoms diffuse into the P(VDF-TrFE) films to passivate the imperfect bonds, leading to a higher intensity of the C_2HF_3 bond, as revealed by the change in the main peak in the F 1 *s* XPS spectra of the P(VDF-TrFE) films from a low to a high binding energy at the depth of 180 nm (Fig. S2c). To characterize the diffusion distance of the fluorine atoms from the n^+-Si wafers to the P(VDF-TrFE) films, *i.e.*, the fluorine-doped P(VDF-TrFE) layer (d_{F_doped}), the XPS PARs of the C_2HF_3 bond related to the raw intensity are calculated and depicted in Fig. 2(f). The typical XPS PAR of the C_2HF_3 bond for the pure P(VDF-TrFE) film is approximately 30%, which is identical to the TrFE mole% of P(VDF-TrFE) powder. With the CF_4 plasma treatment on n^+-Si wafers, the PAR of the C_2HF_3 bond for the P(VDF-TrFE) films is significantly enhanced. The distance from the P(VDF-TrFE) film surface to the position the fluorine atoms diffused, *i.e.*, the pristine P(VDF-TrFE) layer ($d_{pristine}$), can be extracted by the intercept of the slope of the curves at the XPS PAR of the C_2HF_3 bond equal to 30%. The $d_{pristine}$ is found to be 150, 75, and 40 nm for the P(VDF-TrFE) films on 1-, 3- and 5-min CF_4-plasma-treated n^+-Si wafers, respectively. Thus, the d_{F_doped} is obtained according to the following equation,

$$d_{F\_doped} = t_{P(VDF-TrFE)} - d_{pristine} \quad (2)$$

where $t_{P(VDF-TrFE)}$ is the thickness of the P(VDF-TrFE) films on the untreated and CF_4-plasma-treated n^+-Si wafers as depicted in Fig. 2(b).

3.2. Electrical behaviors

In addition to the treatment on n^+-Si wafers, the CF_4 plasma was also performed on the P(VDF-TrFE) films directly to understand the effects of fluorine incorporation (Fig. S3a). The electrical behaviors of the fabricated MFM capacitors were measured and are shown in Fig. S3b. Compared with those with the pure P(VDF-TrFE) film, the MFM capacitors with CF_4-plasma-treated films show worse *P–E* hysteresis characteristics, especially the low remanent polarization values and obvious non-saturated polarization, owing to the severe plasma induced damage. The plasma damage is confirmed by the extremely high leakage current of the CF_4-plasma-treated P(VDF-TrFE) films as revealed by the current versus elec-

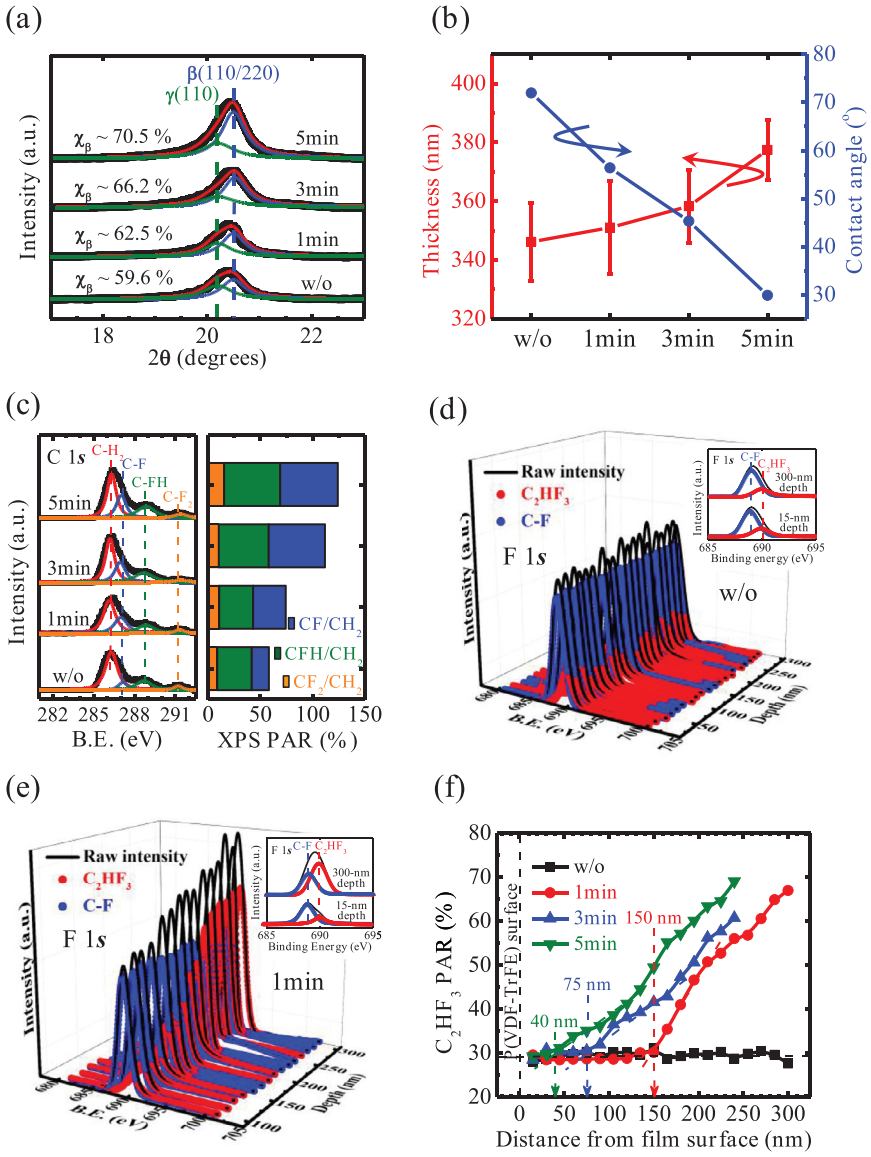

Fig. 2. (a) Curve deconvolution of XRD spectra in 16–24° (2θ) range of the P(VDF-TrFE) films on the untreated and CF_4-plasma-treated n^+-Si wafers. The degree of crystallinity of β and γ-phases is indicated. (b) Statistical distributions of film thickness of the pure and fluorine-incorporated P(VDF-TrFE) films and contact angle of the untreated and CF_4-plasma-treated n^+-Si wafers. (c) C 1*s* XPS spectra and XPS peak-area-ratios (PARs) of C-F, C-FH and C-F_2 bonds related to the C–H_2 bond of the P(VDF-TrFE) films on CF_4-plasma-treated n^+-Si wafers. The depth profiles of the F 1 *s* XPS spectra taken at different etching levels in the P(VDF-TrFE) films on the (d) untreated and (e) 1-min CF_4-plasma-treated n^+-Si wafers. The F 1*s* XPS spectra at 15-nm and 300-nm depth from the P(VDF-TrFE) film surface are shown in inset of these figures. (f) The XPS PARs of the C_2HF_3 bond related to the raw intensity at different distances from the P(VDF-TrFE) film surface of all samples.

tric field (*I*–*E*) characteristics (Fig. S3c) [45]. Therefore, the CF_4 plasma treatment was performed on the n^+-Si wafers instead of the P(VDF-TrFE) films to avoid damage to the copolymers and to obtain the ferroelectric advantages of the incorporation of fluorine into the P(VDF-TrFE) films. Fig. 3(a) shows the *P*–*E* characteristics of the P(VDF-TrFE) MFM capacitors with CF_4-plasma-treated n^+-Si bottom electrodes. The P(VDF-TrFE) MFM capacitor without any treatment presents a typical *P*–*E* hyteresis loop while the samples with CF_4-plasma-treated n^+-Si bottom electrodes show a slightly non-saturated polarization with an increase in the electric field. Some literatures suggested that the non-saturation of polarization of the ferroelectric films is caused by the high leakage current [46,47]. Nonetheless, for the P(VDF-TrFE) films on the CF_4-plasma-treated n^+-Si bottom electrodes, the fluorine atoms diffuse from the n^+-Si wafers into the P(VDF-TrFE) films, contributing to the non-saturated polarization of the film because of the non-uniform polarization and the generation of the depolarization field by the polarization gradient [48]. With an increase in the CF_4 plasma treatment time, the remanent polarization first increases and then decreases; meanwhile, the coercive electric field first decreases and then increases, which can be ascribed to the enhancement in the crystalline β-phase and the increase in the P(VDF-TrFE) film thickness, respectively, as shown in Fig. 2(a) and (b). Thus, the optimal CF_4 plasma treatment time is 1 min (Fig. 3(b)), achieving the highest $2P_r$ of 6.58 μC/cm^2 and the lowest E_c of 0.47 MV/cm. Fig. 3(c) displays the *C*–*E* characteristics of the P(VDF-TrFE) MFM capacitors with CF_4-plasma-treated n^+-Si bottom electrodes measured at a frequency of 1 MHz. The stable butterfly-shaped hysteresis loop indicates the ferroelectric properties of the P(VDF-TrFE) films with fluorine incorporation. Moreover, the permittivity (ε_r) and dielectric loss (tanδ) of the P(VDF-TrFE) MFM capacitors as a function of frequency were measured at the electric field of the largest

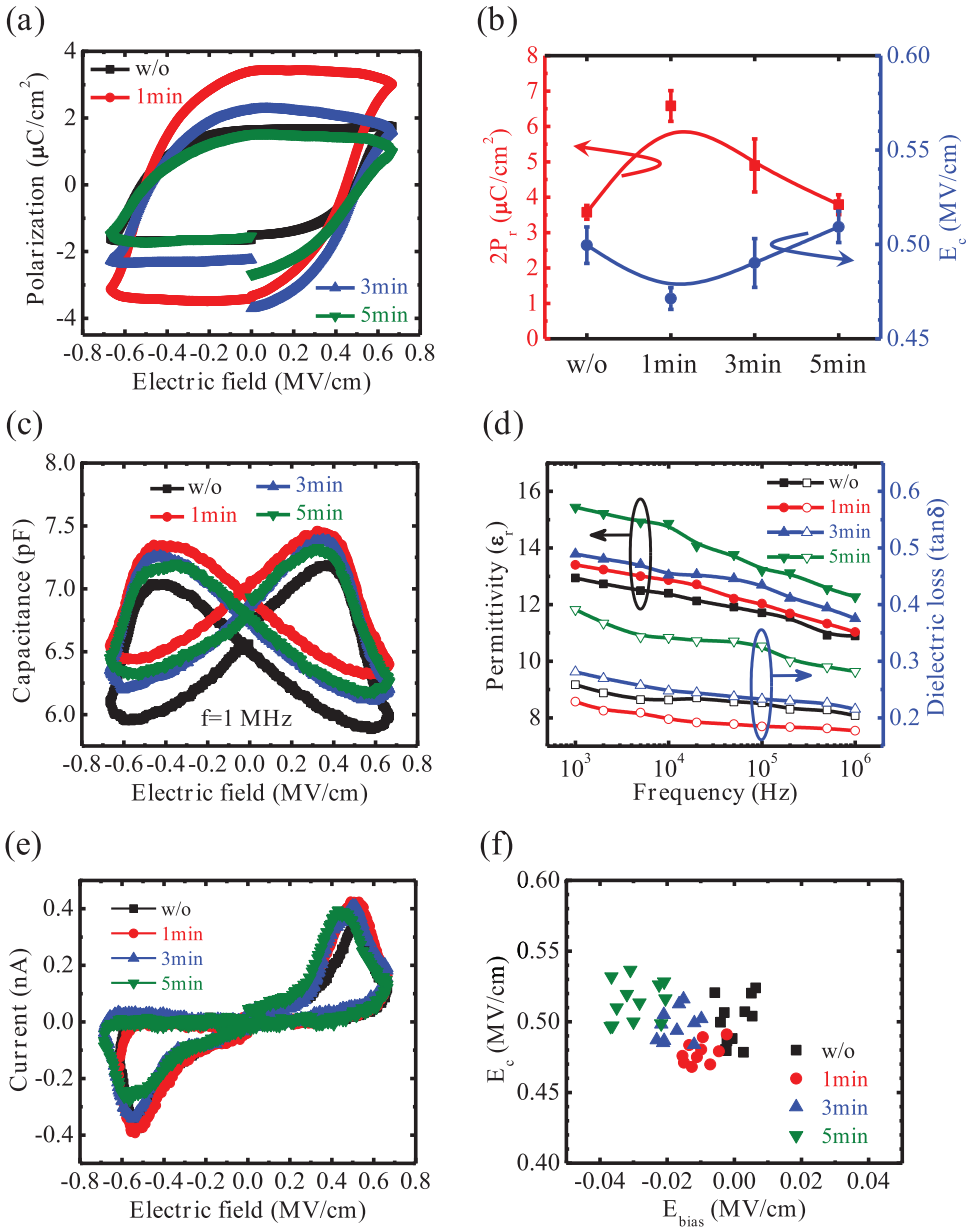

Fig. 3. (a) *P–E* characteristics of the P(VDF-TrFE) MFM capacitors with CF_4-plasma-treated n^+-Si bottom electrodes. (b) Statistical distributions of remanent polarization ($2P_r$) and coercive electric field (E_c) of the P(VDF-TrFE) films on the untreated and CF_4-plasma-treated n^+-Si bottom electrodes. (c) *C–E* characteristics measured at the frequency of 1 MHz of the P(VDF-TrFE) MFM capacitors with CF_4-plasma-treated n^+-Si bottom electrodes. (d) The permittivity (ε_r) and dielectric loss ($\tan\delta$) measured at the bias of the largest capacitance of the P(VDF-TrFE) MFM capacitors as a function of frequency from 1 kHz to 1 MHz. (e) *I–E* hysteresis loops of the P(VDF-TrFE) MFM capacitors with CF_4-plasma-treated n^+-Si bottom electrodes. (f) Switching mapping as a function of E_{bias} and E_c for the P(VDF-TrFE) films on the untreated and CF_4-plasma-treated n^+-Si bottom electrodes.

capacitance and are shown in Fig. 3(d). All samples exhibit an obvious decreasing trend of dielectric permittivity in the frequency range from 1 kHz to 1 MHz as a result of the delayed response of the β-phase against the switching speed of the applied electric field. It is worth noting that a permittivity at the frequency of 1 MHz increases from 10.89 for the pure P(VDF-TrFE) films to 12.28 for the films on the 5-min CF_4-plasma-treated n^+-Si bottom electrode, thanks to the increase in the C_2HF_3 bond as proposed by Xia et al. [27]. As a consequence, a reduced dielectric loss can be observed for the P(VDF-TrFE) films on the 1-min CF_4-plasma-treated n^+-Si bottom electrode, as shown in Fig. 3(d), improving the characteristics of well-known ferroelectric relaxation because of the enhancement in crystallinity [49] and the reduction in defects and imperfections within the P(VDF-TrFE) copolymer chains [50], as shown in Fig. 2. However, for the films on the CF_4-plasma-treated n^+-Si bottom electrodes with a longer plasma treatment time, a higher dielectric loss is observed due to the higher ferroelectric leakage current [51], which will be discussed later. Fig. 3(e) shows the *I–E* hysteresis loops of the P(VDF-TrFE) films on the CF_4-plasma-treated n^+-Si bottom electrodes. By contrast, the fluorine-incorporated P(VDF-TrFE) films show quite distinctive *I–E* curves compared to that of the pure P(VDF-TrFE) film. The switching peaks in both positive and negative electric field regions shift toward the negative direction, suggesting the asymmetric behaviors of the fluorine-incorporated P(VDF-TrFE) films [52]. Here, the E_c value can be calculated from Eq. (3), where the peaks observed in the positive and negative electric field regions of Fig. 3(e) correspond to the positive-switching field (E_{ps}) and negative-switching

field (E_{ns}), respectively.

$$E_c = \frac{E_{ps} - E_{ns}}{2} \tag{3}$$

For the pure P(VDF-TrFE) film, the absolute magnitude of E_{ps} and E_{ns} can be found to be identical. If the magnitudes of E_{ps} and E_{ns} are not identical, the film might contain a non-uniform ferroelectric polarization most likely due to the asymmetric film composition, which induces a non-uniform field distribution. Thus, the internal bias field (E_{bias}) is defined to identify the uniformity of electric field and can be obtained according to the following equation:

$$E_{bias} = \frac{E_{ps} + E_{ns}}{2} \tag{4}$$

In Fig. 3(f), the switching map is plotted as a function of E_{bias} and E_c for the P(VDF-TrFE) films. For the pure P(VDF-TrFE) film, there is no notable internal E_{bias}; *i.e.*, the data would appear around $E_{bias} = 0$, meaning that the composition of the film is uniform. However, the E_{bias} gradually shifts toward the negative direction for the fluorine-incorporated P(VDF-TrFE) films, *e.g.*, $E_{bias} = -0.03$ MV/cm for the samples with 5-min CF_4-plasma-treated n^+-Si bottom electrode. The negative shift could be ascribed to the asymmetric polarization of the P(VDF-TrFE) film, which is accompanied by the non-uniform C_2HF_3 bond distribution, as revealed in Fig. 2(f), leading to the non-saturated polarization of *P–E* hysteresis loops (Fig. 3(a)).

Fig. 4(a) depicts the leakage current versus the electric field (I_L–E) characteristics of the P(VDF-TrFE) MFM capacitors with CF_4-plasma-treated n^+-Si bottom electrodes measured at room temperature. For the fluorine-incorporated P(VDF-TrFE) films, an increase in leakage current is observed, especially for samples under a positive TE bias, which is responsible for the higher dielectric loss shown in Fig. 3(d). It is reported that the carrier transport mechanism of the MFM capacitors with P(VDF-TrFE) films can be ascribed to Schottky emission, Frenkel–Poole (*F–P*) emission, and space-charge-limited-current (SCLC) conduction depending on the different measurement temperatures [52]. To understand the charge trapping levels of the pure and fluorine-incorporated P(VDF-TrFE) films, the leakage currents of the MFM capacitors were measured at 213–273 K and are shown in Figs. 4(b) and S4a,c,e. Then, the current density divided by the electric field (J/E) as a function of the measured temperature at positive and negative TE biases is also plotted and presented in the inset figure of Figs. 4(b) and S4b,d,f. The linear fit of the curve means that the dominant carrier transport mechanism of the P(VDF-TrFE) MFM capacitors is *F–P* emission, as expressed by the following equation:

$$J \propto E \times \exp\left(\frac{-q\left(\varphi_t - \sqrt{qE/\pi\varepsilon}\right)}{k_B T}\right) \tag{5}$$

where T is the absolute temperature, κ_B is the Boltzmann constant, q is the electric charge, E is the electric field, ε is the permittivity, and φ_t is the charge trapping level of the P(VDF-TrFE) films. The permittivity of the P(VDF-TrFE) films on the untreated and CF_4-plasma-treated n^+-Si bottom electrodes is approximately 11–12 as presented in Fig. 3(d). To obtain the charge trapping levels, the slopes of the curves in the inset figure of Figs. 4(b) and S4b,d,f were calculated as the equivalent charge trapping energy ($E_{act} = -q[\varphi_t - (qE/\pi\varepsilon)^{1/2}]$), and the E_{act} versus $E^{1/2}$ curve is plotted in Fig. 4(c). By extrapolating the curve to the y-axis, the charge trapping level at a positive TE bias; *i.e.*, the bottom electrode injection, of the pure P(VDF-TrFE) film can be determined to be 0.253 eV, which is larger than that of the fluorine-incorporated films for 0.154 – 0.226 eV. Thus, it can be concluded that the fluorine atoms can passivate the deep traps of the P(VDF-TrFE) films. It is important to note that the charge trapping levels of the fluorine-incorporated P(VDF-TrFE) films for the BE injection are lower than those for the TE injection (negative TE bias), implying that the fluorine atoms are diffused from the n^+-Si bottom electrode.

To obtain a physical insight into the polarization of the P(VDF-TrFE) films on the CF_4-plasma-treated n^+-Si bottom electrodes, we consider the device with a pristine P(VDF-TrFE) layer ($d_{pristine}$) on the top and fluorine-doped P(VDF-TrFE) layer (d_{F_doped}) on the bottom of the bilayer film as an ideal bilayer capacitor. The thicknesses of these two layers can be determined by XPS depth profiling (Fig. 2(f)) and are obtained using Eq. (2). For a voltage applied across the bilayer capacitor, the potential drop across these two ferroelectric layers and the corresponding charge on the electrodes can be calculated. At the pristine and fluorine-doped P(VDF-TrFE) interface, the following charge equality equation applies [29]:

$$\frac{\varepsilon_0 V_{fp}}{d_{pristine}} + P_{fp} = \frac{\varepsilon_0 (V_a - V_{fp})}{d_{F\_doped}} + (P_{ft} - P_{fp}) \tag{6}$$

where $d_{pristine}$ and d_{F_doped} are the thicknesses of pristine and fluorine-doped P(VDF-TrFE) layer, respectively; V_{fp} and V_a are the voltage drops across the pristine P(VDF-TrFE) layer and the applied voltage, respectively; P_{fp} and P_{ft} are the polarization in the pristine P(VDF-TrFE) layer and total polarization value, respectively; and ε_0 is the vacuum permittivity of 8.854×10^{-14} F/cm. To obtain the polarization values of the pristine and fluorine-doped P(VDF-TrFE) layers, the *P–V* curves of single-layer P(VDF-TrFE) capacitors for thicknesses of 290, 380 and 520 nm were measured and are shown in Fig. S5. In the bilayer capacitors, the thicknesses of pristine P(VDF-TrFE) layer for the samples with 1-, 3- and 5-min CF_4-plasma-treated n^+-Si bottom electrodes were 150, 75, and 40 nm, respectively. Therefore, the polarization P_{fp} of each of the sample can be determined by the characteristics of P_f as a function of V_f with different thicknesses (Fig. 4(d)) and scaled for several thicknesses used in the different bilayer capacitors. For $V_a = 20$ V and P_f versus V_f curves in Fig. 4(d), the solution of Eq. (6) yields V_{fp} as 11.31, 8.6 and 6.44 V and the corresponding voltage drop across the fluorine-doped P(VDF-TrFE) layers; *i.e.*, $V_a - V_{fp}$, as 8.69, 11.4 and 13.56 V, and the electrode charge density in fluorine-doped P(VDF-TrFE) layers; *i.e.*, $P_{ft} - P_{fp}$, as 3.544, 2.699 and 2.386 μC/cm^2, for the samples with 1-, 3- and 5-min CF_4-plasma-treated n^+-Si bottom electrodes, respectively. The enhanced electrode charge density in the fluorine-doped P(VDF-TrFE) layer indicates that more polarization of the film can provide better ferroelectric properties, as shown in the three-dimensional (3D) $2P_r$ contour plot in Fig. 4(e), compared with those of the pristine layer. Next, the cycling stabilities of the P(VDF-TrFE) films on the CF_4-plasma-treated n^+-Si bottom electrodes were examined in detail. Fig. 4(f) demonstrates the endurance behaviors of the P(VDF-TrFE) MFM capacitors measured at a pulse electric field of 0.5 MV/cm for 0.5 s. An obvious drop of 34% in $2P_r$ for pure P(VDF-TrFE) samples is observed after 3×10^4 switching cycles. For the samples with 1-min CF_4-plasma-treated n^+-Si bottom electrode, a negligible polarization fatigue of less than 6% in the same period is achieved due to the reduction in defects and imperfections within the P(VDF-TrFE) copolymer chains and at the crystallite boundaries [53,54]. However, too much fluorine incorporation in the P(VDF-TrFE) film contributes to a higher injection of electrons from the n^+-Si bottom electrode, as revealed in Fig. 4(a), increasing the amount of charge trapping and hence fatigue [55]. All material and electrical characteristics of the P(VDF-TrFE) MFM capacitors with CF_4-plasma-treated n^+-Si bottom electrodes obtained above are summarized in Table 1.

3.3. Chemical reaction schematics and energy band diagrams

Fig. 5(a) and (b) shows the chemical structures of the P(VDF-TrFE) films on the untreated and CF_4-plasma-treated n^+-Si bottom

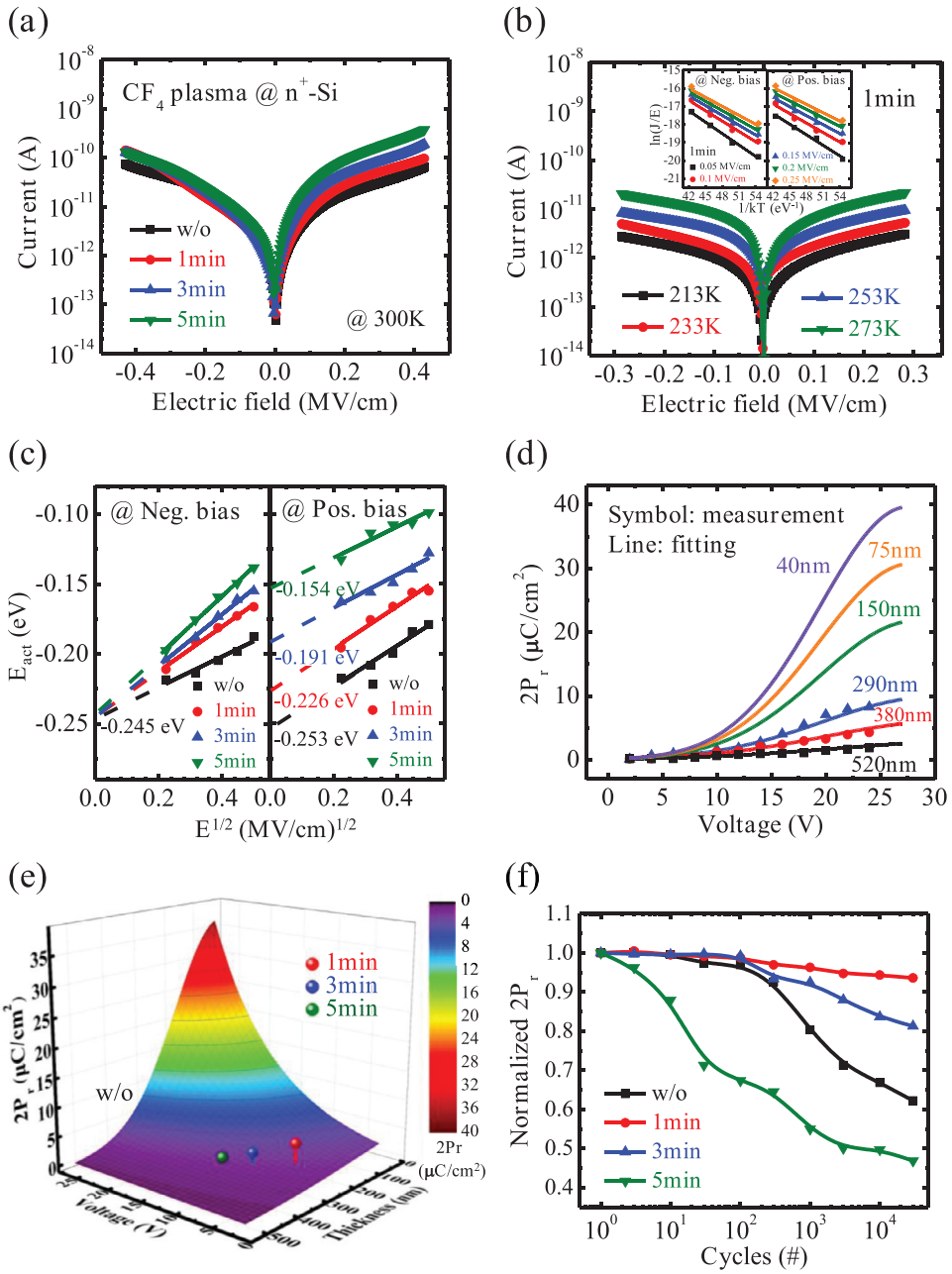

Fig. 4. (a) I_L–E characteristics of the P(VDF-TrFE) MFM capacitors with CF_4-plasma-treated n^+-Si bottom electrodes measured at room temperature. (b) I_L–E characteristics measured at 213 – 273 K of the P(VDF-TrFE) MFM capacitors with 1-min CF_4-plasma-treated n^+-Si bottom electrode. The current density divided by the electric field (J/E) as a function of the measured temperature at positive and negative TE biases is plotted in the inset of this figure. (c) The equivalent charge trapping energy (E_{act}) versus $E^{1/2}$ curves at positive and negative TE biases. (d) The characteristics of P_f as a function of V_f with different thicknesses of P(VDF-TrFE) films (290, 380, and 520 nm) and scaled for several thicknesses used in bilayer capacitors (40, 75, and 150 nm). (e) 3D $2P_r$ contour plot of the P(VDF-TrFE) MFM capacitors with different operation voltages and film thicknesses. The $2P_r$ of P(VDF-TrFE) films on 1-, 3- and 5-min CF_4-plasma-treated n^+-Si bottom electrodes are also shown in this figure. (f) The endurance behaviors of P(VDF-TrFE) MFM capacitors measured at the pulse electric field of 0.5 MV/cm for 0.5 s.

Table 1
Summary of material and electrical characteristics of the P(VDF–TrFE) MFM capacitors with CF_4-plasma-treated n^+-Si bottom electrodes.

Para./Split	Film thickness (nm)	Contact angle (○)	d_{F_doped} (nm)	Relative permittivity @ 1 MHz (ε_r)	Dielectric loss @ 1 MHz (tanδ)	$2P_r$ (μC/cm^2)	E_c (MV/cm)	E_{bias} (MV/cm)	$q\varphi_t$ @ pos. TE bias (eV)	$q\varphi_t$ @ neg. TE bias (eV)	Polarization fatigue @ 3 × 10^4 cycles (%)
w/o	346.17	72	–	10.89	0.204	3.574	0.498	0.0002	0.253	0.245	38
1 min	**351.00**	**56**	**201**	**11.03**	**0.177**	**6.578**	**0.471**	**−0.0101**	**0.226**	**0.244**	**6**
3 min	358.20	45	283	11.51	0.215	4.897	0.492	−0.0173	0.191	0.245	19
5 min	377.46	32	337	12.28	0.282	3.789	0.509	−0.0293	0.154	0.244	53

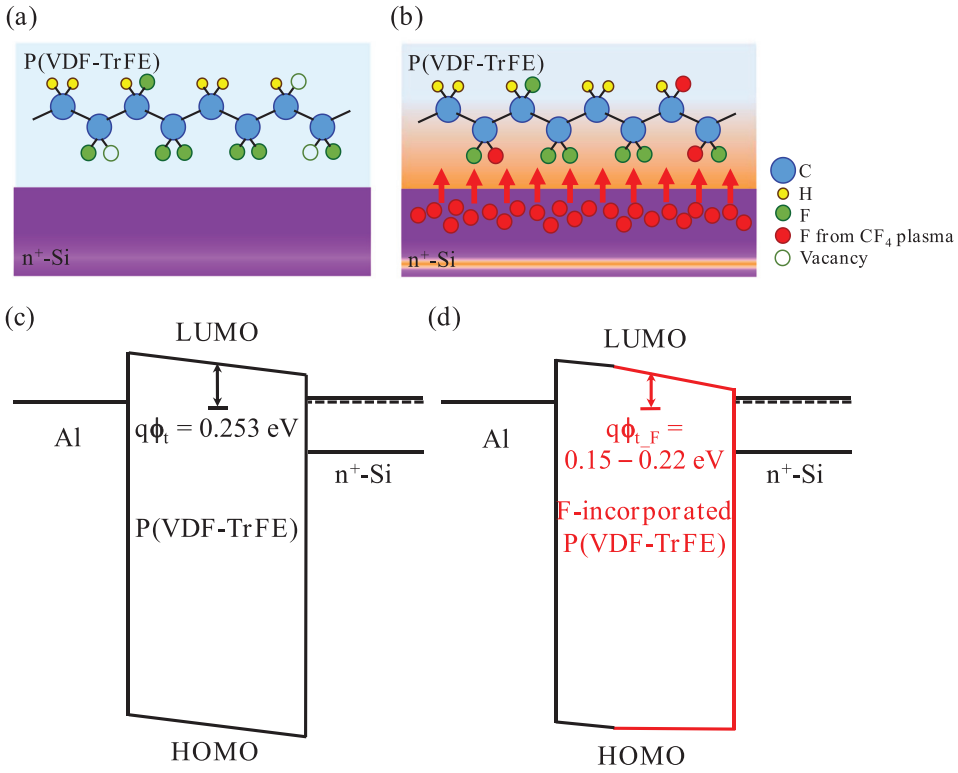

Fig. 5. Illustration of the chemical structures of the P(VDF-TrFE) films on the (a) untreated and (b) CF_4-plasma-treated n^+-Si bottom electrodes. Energy band diagrams with charge trapping levels of the P(VDF-TrFE) films on the (c) untreated and (d) CF_4-plasma-treated n^+-Si bottom electrodes.

electrodes respectively. P(VDF-TrFE) is a crystalline copolymer in which monomer units of PVDF (–CH_2–CF_2–) and TrFE (–CF_2–CFH–) are connected. However, there are some defects and imperfections within the P(VDF-TrFE) copolymer chains, as shown in Fig. 5(a), leading to the capture of charges and hindering the switchable polarization. For a P(VDF-TrFE) film on the CF_4-plasma-treated n^+-Si bottom electrode (Fig. 5(b)), the fluorine atoms can diffuse from the Si wafer to the P(VDF-TrFE) film during annealing, passivating the imperfections and increasing the number of C_2HF_3 bonds in the P(VDF-TrFE) film, as examined by the XPS analysis in Fig. 2. Thus, the ferroelectric behaviors of the P(VDF-TrFE) films on the CF_4-plasma-treated n^+-Si bottom electrodes are significantly enhanced, as revealed in Fig. 3. The energy band diagrams of the Al/P(VDF-TrFE)/n^+-Si MFM structures with the untreated and CF_4-plasma-treated n^+-Si bottom electrodes at thermal equilibrium are illustrated in Fig. 5(c) and (d), respectively. The charge trapping levels obtained from Fig. 4(c) are also illustrated in this figure. As shown in Fig. 5(b), the CF_4 plasma treatment on n^+-Si bottom electrodes can increase the number of C_2HF_3 bonds in the P(VDF-TrFE) film, thereby enhancing the percentage of TrFE in the P(VDF-TrFE) film, especially the part of the film near the P(VDF-TrFE)/n^+-Si interface. Consequently, the energy band gap at the bottom of the fluorine-incorporated P(VDF-TrFE) film is smaller than that of the pristine P(VDF-TrFE) film [56,57]. The modified energy band diagram and charge trapping level of the P(VDF-TrFE) films on the CF_4-plasma-treated n^+-Si bottom electrodes are responsible for the enhancement in the aforementioned electrical behaviors shown in Figs. 3 and 4.

4. Conclusion

In this study, P(VDF-TrFE) MFM capacitors with CF_4-plasma-treated n^+-Si wafers as BEs were developed. The fluorine-incorporated P(VDF-TrFE) copolymers are identified using XPS depth profiling and XRD analysis. By examining the *I–V* curves, an asymmetric P(VDF-TrFE) film due to the enrichment in C_2HF_3 (trifluoroethylene) bonds and the increase in the β-phase at the bottom of the film is found. Hence, the charge trapping level of 0.154–0.226 eV for BE injection was extracted from the *F–P* emission at 213 – 273 K, which is lower than that for the TE injection. To enhance the ferroelectric behaviors of P(VDF-TrFE) MFM capacitors, n^+-Si bottom electrode subjected to the CF_4 plasma treatment for 1 min are found to exhibit a large remanent polarization of 6.58 μC/cm^2, a low coercive electric field of 0.47 MV/cm, and excellent endurance for more than 3×10^4 cycles with negligible fatigue. The fluorine-incorporated P(VDF-TrFE) copolymers offer a material for high-performance ferroelectric memory that can be integrated into organic electronics.

Declaration of Competing Interest

The authors declare that they have no known competing financial interests or personal relationships that could have appeared to influence the work reported in this paper.

Acknowledgments

This research was supported by Ministry of Science and Technology, R.O.C (Contract Nos. of MOST 105-2628-E-182-001-MY3, MOST 106-2632-E-182-001, MOST 107-2218-E-182-007, and 106-2221-E-182-057-MY3), Chang Gung Memorial Hospital, Linkou, Taiwan (Contract Nos. of CMRPD2F0123, CMRPD2H0131, and BMRPA74) and Chang Gung University (QZRPD181).

Supplementary materials

Supplementary material associated with this article can be found, in the online version, at doi:10.1016/j.jtice.2019.11.005.

References

[1] Sumi T, Judai Y, Hirano K, Ito T, Mikawa T, Takeo M, Azuma M, Hayashi SI, Uemoto Y, Arita K, Nasu T, Nagano Y, Inoue A, Matsuda A, Fuji E, Shimada Y, Otsuki T. Ferroelectric nonvolatile memory technology and its applications. Jpn J Appl Phys 1996;35:1516–20.

[2] Grachova Y, Vollebregt S, Lacaita AL, Sarro PM. High quality wafer-scale CVD graphene on molybdenum thin film for sensing application. Procedia Eng 2014;87:1501–4.

[3] Du CH, Zhu BK, Xu YY. Effects of stretching on crystalline phase structure and morphology of hard elastic PVDF fibers. J Appl Polym Sci 2007;104:2254–9.

[4] Mandal D, Yoon S, Kim KJ. Origin of piezoelectricity in an electrospun poly(vinylidene fluoride-trifluoroethylene) nanofiber web-based nanogenerator and nano-pressure sensor. Macromol Rapid Commun 2011;32:831–7.

[5] Bhavanasi V, Kusuma DY, Lee PS. Polarization orientation, piezoelectricity, and energy harvesting performance of ferroelectric PVDF-TRFE nanotubes synthesized by nanoconfinement. Adv Energy Mater 2014;4:1400723.

[6] Kawai H. The piezoelectricity of poly (vinylidene fluoride). Jpn J Appl Phys 1969;8:975–6.

[7] Yamada T. Piezoelectricity of a vinylidene fluoride-trifluoroethylene copolymer. J Appl Phys 1982;53:6335–9.

[8] Ruan L, Yao X, Chang Y, Zhou L, Qin G, Zhang X. Properties and applications of the β phase poly(vinylidene fluoride). Polymers (Basel) 2018;10:228.

[9] Furukawa T. Ferroelectric properties of vinylidene fluoride copolymers. Phase Transit 1989;18:143–211.

[10] Mao D, Gnade B, Quevedo-Lopez M. Ferroelectric properties and polarization switching kinetic of poly (vinylidene fluoride-trifluoroethylene) copolymer. In: Lallart M, editor. Ferroelectrics – Physical effects. Croatia: IntechOpen; 2011. p. 77–100.

[11] Valiyaneerilakkal U, Varghese S. Poly (vinylidene fluoride-trifluoroethylene)/barium titanate nanocomposite for ferroelectric nonvolatile memory devices. AIP Adv 2013;3:042131.

[12] Park JH, Kurra N, AlMadhoun MN, Odeh IN, Alshareef HN. A two-step annealing process for enhancing the ferroelectric properties of poly(vinylidene fluoride) (PVDF) devices. J Mater Chem C 2015;3:2366–70.

[13] Salimi A, Yousefi AA. Analysis method: ftir studies of β-phase crystal formation in stretched PVDF films. Polym Test 2003;22:699–704.

[14] Mahdi IR, Gan CW, Majid HW. Hot plate annealing at a low temperature of a thin ferroelectric P(VDF-TrFE) film with an improved crystalline structure for sensors and actuators. Sensors 2014;14.

[15] Gomes J, Serrado Nunes J, Sencadas V, Lanceros-Mendez S. Influence of the β-phase content and degree of crystallinity on the piezo- and ferroelectric properties of poly(vinylidene fluoride). Smart Mater Struct 2010;19:065010.

[16] Qiu X. Patterned piezo-, pyro-, and ferroelectricity of poled polymer electrets. J Appl Phys 2010;108:011101.

[17] Bolton JR. The nature of the chemical bond and the structure of molecules and crystals: an introduction to modern structural chemistry. Science 1984.

[18] Salimi A, Yousefi AA. Conformational changes and phase transformation mechanisms in PVDF solution-cast films. J Polym Sci B 2004;42:3487–95.

[19] Fujisaki S, Ishiwara H, Fujisaki Y. Low-voltage operation of ferroelectric poly(vinylidene fluoride-trifluoroethylene) copolymer capacitors and metal-ferroelectric-insulator-semiconductor diodes. Appl Phys Lett 2007;90:162902.

[20] Jain A, Jayanth Kumar S, Roy Mahapatra D, Rathod V. Development of P(VDF-TrFE) films and its quasi-static and dynamic strain response. Int J Adv Res Technol 2013;2 2598-05.

[21] Costa LMM, Bretas RES, Gregorio R. Effect of solution concentration on the electrospray/electrospinning transition and on the crystalline phase of PVDF. Mater Sci Appl 2010;01:247–52.

[22] Ducrot PH, Dufour I, Ayela C. Optimization of pvdf-trfe processing conditions for the fabrication of organic mems resonators. Sci Rep 2016;6:19426.

[23] Hahm SW, Khang DY. Crystallization and microstructure-dependent elastic moduli of ferroelectric P(VDF-TrFE) thin films. Soft Matter 2010;6:5802–6.

[24] Kim S, Towfeeq I, Dong Y, Gorman S, Rao MA, Koley G. P(VDF-TrFE) film on pdms substrate for energy harvesting applications. Appl Sci 2018;8:213.

[25] Chen X, Tian H, Li X, Shao J, Ding Y, An N, Zhou Y. A high performance P(VDF-TrFE) nanogenerator with self-connected and vertically integrated fibers by patterned EHD pulling. Nanoscale 2015;7:11536–44.

[26] Lou Z, Chen S, Wang L, Jiang K, Shen G. An ultra-sensitive and rapid response speed graphene pressure sensors for electronic skin and health monitoring. Nano Energy 2016;23:7–14.

[27] Xia W, Wang Z, Xing J, Cao C, Xu Z. The dependence of dielectric and ferroelectric properties on crystal phase structures of the hydrogenized P(VDF-TrFE) films with different thermal processing. IEEE Trans Ultrason Ferroelectr Freq Control 2016;63:1674–80.

[28] Hu J, Zhang J, Fu Z, Jiang Y, Ding S, Zhu G. Solvent vapor annealing of ferroelectric P(VDF-TrFE) thin films. ACS Appl Mater Interfaces 2014;6:18312–18.

[29] Singh D, Deepak, Garg A. Interface morphology driven control of electrical properties of P(VDF-TrFE) and pmma blend M–I–M capacitors. Org Electron 2014;15:3811–17.

[30] Tsutsumi N, Kosugi R, Kinashi K, Sakai W. Nature of the enhancement in ferroelectric properties by gold nanoparticles in vinylidene fluoride and trifluoroethylene copolymer. ACS Appl Mater Interfaces 2016;8:16816–22.

[31] Mai M, Ke S, Lin P, Zeng X. Intrinsic and extrinsic effects on the ferroelectric switching of thin poly(vinylidene fluoride/trifluoroethylene) copolymer films. APL Mater 2016;4:046107.

[32] Singh D, Deepak, Garg A. An efficient route to fabricate fatigue-free P(VDF-TrFE) capacitors with enhanced piezoelectric and ferroelectric properties and excellent thermal stability for sensing and memory applications. Phys Chem Chem Phys 2017;19:7743–50.

[33] Xia W, Zhang Z. PVDF-based dielectric polymers and their applications in electronic materials. IET Nanodielectr 2018;1:17–31.

[34] Scott JF, Kammerdiner L, Parris M, Traynor S, Ottenbacher V, Shawabkeh A, Oliver WF. Switching kinetics of lead zirconate titanate submicron thin-film memories. J Appl Phys 1988;64:787–92.

[35] Fukunaga M, Noda Y. New technique for measuring ferroelectric and antiferroelectric hysteresis loops. J Phys Soc Jpn 2008;77:064706.

[36] Ghosh SK, Alam MM, Mandal D. The in situ formation of platinum nanoparticles and their catalytic role in electroactive phase formation in poly(vinylidene fluoride): a simple preparation of multifunctional poly(vinylidene fluoride) films doped with platinum nanoparticles. RSC Adv 2014;4:41886–94.

[37] Garain S, Jana S, Sinha TK, Mandal D. Design of in situ poled Ce^{3+}-doped electrospun PVDF/graphene composite nanofibers for fabrication of nanopressure sensor and ultrasensitive acoustic nanogenerator. ACS Appl Mater Interfaces 2016;8:4532–40.

[38] Roy K, Ghosh SK, Sultana A, Garain S, Xie M, Bowen CR, Henkel K, Schmeiβer D, Mandal D. A self-powered wearable pressure sensor and pyroelectric breathing sensor based on Go interfaced PVDF nanofibers. ACS Appl Nano Mater 2019;2:2013–25.

[39] Iqbal M, Dinh DK, Abbas Q, Imran M, Sattar H, Ahmad AU. Controlled surface wettability by plasma polymer surface modification. Surfaces 2019;2:349–71.

[40] Bachmann J, Horton R, van der Ploeg RR, Woche S. Modified sessile drop method for assessing initial soil–water contact angle of sandy soil. Soil Sci Soc Am J 2000;64:564–7.

[41] Wang JC, Karmakar RS, Lu YJ, Wu MC, Wei KC. Nitrogen plasma surface modification of poly(3,4-ethylenedioxythiophene):poly(styrenesulfonate) films to enhance the piezoresistive pressure-sensing properties. J Phys Chem C 2016;120:25977–84.

[42] Tressaud A. Functionalized inorganic fluorides: Synthesis, characterization & properties of nanostructured solids. New Jersey: Wiley; 2010.

[43] Xu B, Borca CN, Ducharme S, Sorokin AV, Dowben PA, Fridkin VM, Palto SP, Petukhova NN, Yudin SG. Aluminum doping of poly(vinylidene fluoride with trifluoroethylene) copolymer. J Chem Phys 2001;114:1866–9.

[44] Lei YG, Ng KM, Weng LT, Chan CM, Li L. XPS C 1s binding energies for fluorocarbon–hydrocarbon microblock copolymers. Surf Interface Anal 2003;35:852–5.

[45] Wang JC, Lin C-T. CF_4 plasma treatment on nanostructure band engineered gd2o3-nanocrystal nonvolatile memory. J Appl Phys 2011;109:064506.

[46] Goel S, Sinha N, Yadav H, Godara S, Joseph AJ, Kumar B. Ferroelectric gd-doped zno nanostructures: enhanced dielectric, ferroelectric and piezoelectric properties. Mater Chem Phys 2017;202:56–64.

[47] Qiao Y, Zhou Y, Wang S, Yuan L, Du Y, Lu D, Che G, Che H. Composition dependent magnetic and ferroelectric properties of hydrothermally synthesized $gdfe_{1-x}cr_xo_3$ ($0.1 \leq x \leq 0.9$) perovskites. Dalton Trans 2017;46:5930–7.

[48] Zhao H, Kimura H, Yao Q, Du Y, Cheng Z, Wang XLallart M, editor. New multiferroic materials: Bi_2FeMnO_6.. Ferroelectrics – Material Aspects 2011:237–50.

[49] Fang L, Shen M, Yang J, Li Z. Reduced dielectric loss and leakage current in $CaCu_3Ti_4O_{12}/SiO_2/CaCu_3Ti_4O_{12}$ multilayered films. Solid State Commun 2006;137:381–6.

[50] Tsai MS, Tseng TY. Effect of bottom electrodes on dielectric relaxation and defect analysis of $(Ba_{0.47}Sr_{0.53})TiO_3$ thin film capacitors. Mater Chem Phys 1998;57:47–56.

[51] Chernikova AG, Kozodaev MG, Negrov DV, Korostylev EV, Park MH, Schroeder U, Hwang CS, Markeev AM. Improved ferroelectric switching endurance of La-doped $Hf_{0.5}Zr_{0.5}O_2$ thin films. ACS Appl Mater Interfaces 2018;10:2701–8.

[52] Zhao XL, Wang JL, Tian BB, Liu BL, Zou YH, Wang XD, Sun S, Sun JL, Meng XJ, Chu JH. Temperature dependence of electronic transport property in ferroelectric polymer films. Appl Surf Sci 2014;316:497–500.

[53] Zhao D, Katsouras I, Li M, Asadi K, Tsurumi J, Glasser G, Takeya J, Blom PWM, de Leeuw DM. Polarization fatigue of organic ferroelectric capacitors. Sci Rep 2014;4:5075.

[54] Zeng ZG, Zhu GD, Zhang L, Yan XJ. Effect of crystallinity on polarization fatigue of ferroelectric P(VDF-TrFE) copolymer films. Chin J Polym Sci 2009;27:479–85.

[55] Khan MA, Bhansali US, Almadhoun MN, Odeh IN, Cha D, Alshareef HN. High-performance ferroelectric memory based on phase-separated films of polymer blends. Adv Funct Mater 2014;24:1372–81.

[56] Mandal D, Henkel K, Müller K, Schmeißer D. Bandgap determination of P(VDF-TrFE) copolymer film by electron energy loss spectroscopy. Bull Mater Sci 2010;33:457–61.

[57] Bystrov VS, Paramonova EV, Dekhtyar Y, Pullar RC, Katashev A, Polyaka N, Bystrova AV, Sapronova AV, Fridkin VM, Kliem H, Kholkin AL. Polarization of poly(vinylidene fluoride) and poly(vinylidene fluoride-trifluoroethylene) thin films revealed by emission spectroscopy with computational simulation during phase transition. J Appl Phys 2012;111:104113.